Supplementary Information (SI) for Journal of Materials Chemistry A.

Shaping Nanoparticle-Based Aerogels for Efficient Light-Driven Catalysis

Fabian Matter[#], *David Kiwic*[#], *Marco Bernet, Elena Tervoort, Markus Niederberger**

Laboratory for Multifunctional Materials, Department of Materials, ETH Zurich, Vladimir-Prelog-Weg 5, 8093 Zurich, Switzerland

[#] These authors contributed equally to the work.

* Corresponding author: markus.niederberger@mat.ethz.ch

SUPPLEMENTARY INFORMATION

Photocatalytic measurements

Figure S1 illustrates the photocatalytic measurement setup, featuring the custom-built photoreactor.[1] The gas preparation unit enables precise control of methanol concentration in the gas stream across varying flow rates. This methanol-enriched stream is directed through the photoreactor, where the aerogel sample is illuminated from both sides by LEDs, and the resulting product stream is analyzed by gas chromatography.

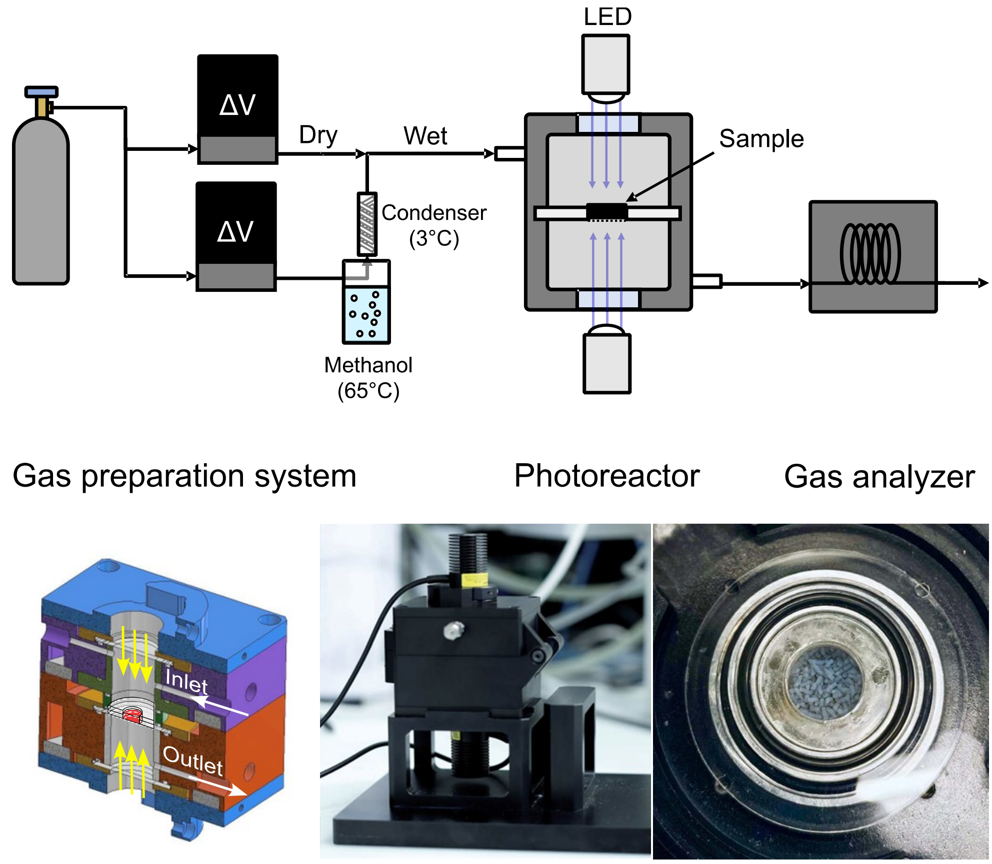

Figure S1 Top: Schematic of the photocatalytic reaction setup, including gas flow controllers and a vaporization system that feeds a methanol-enriched air stream into the photoreactor. The outflow is analyzed using a gas chromatograph. Bottom Left: Cross-section of the photoreactor with the catalyst bed highlighted in red. Bottom Middle: Digital image of the custom-built photoreactor. Bottom Right: Hollow plastic cylinder containing Pd/TiO_2 worm-shaped granules on a wire mesh.

The procedure for obtaining the relevant photocatalytic data involved fixing the methanol concentration and total reactant gas flow rate while systematically varying the light intensity (irradiance). The irradiance was incrementally increased in 200 mW/cm^2 steps (from 200 to 2000 mW/cm^2) and then decreased again to assess stability and reproducibility. Each setting was maintained for 60 minutes to allow for equilibration, with the reactor outgas analyzed by gas chromatography every ~7 minutes. As an example, **Figure S2** shows a measurement for the monolithic aerogel under a 20 SCCM flow of air containing 3 % methanol. To estimate the catalyst's stability, we compared the STY under 200 mW/cm^2 irradiation in the first and last hour of testing under identical conditions, separated by approximately 15 hours of high-conversion photocatalysis. A slight activity decline from 11.0 to 10.7 mmol g^{-1} h^{-1} was observed, corresponding to a deactivation rate of approximately 0.2 % per hour. This minor decrease is attributed to coke deposition, a common deactivation mechanism in VOC decomposition. Additionally, the formaldehyde detected at lower light intensities is known to polymerize, potentially accelerating catalyst fouling. Therefore, operating at higher light intensities, which promote more complete methanol oxidation, should be preferred. Complete oxidation to CO_2 minimizes coking and enhances the long-term stability of the photocatalyst.

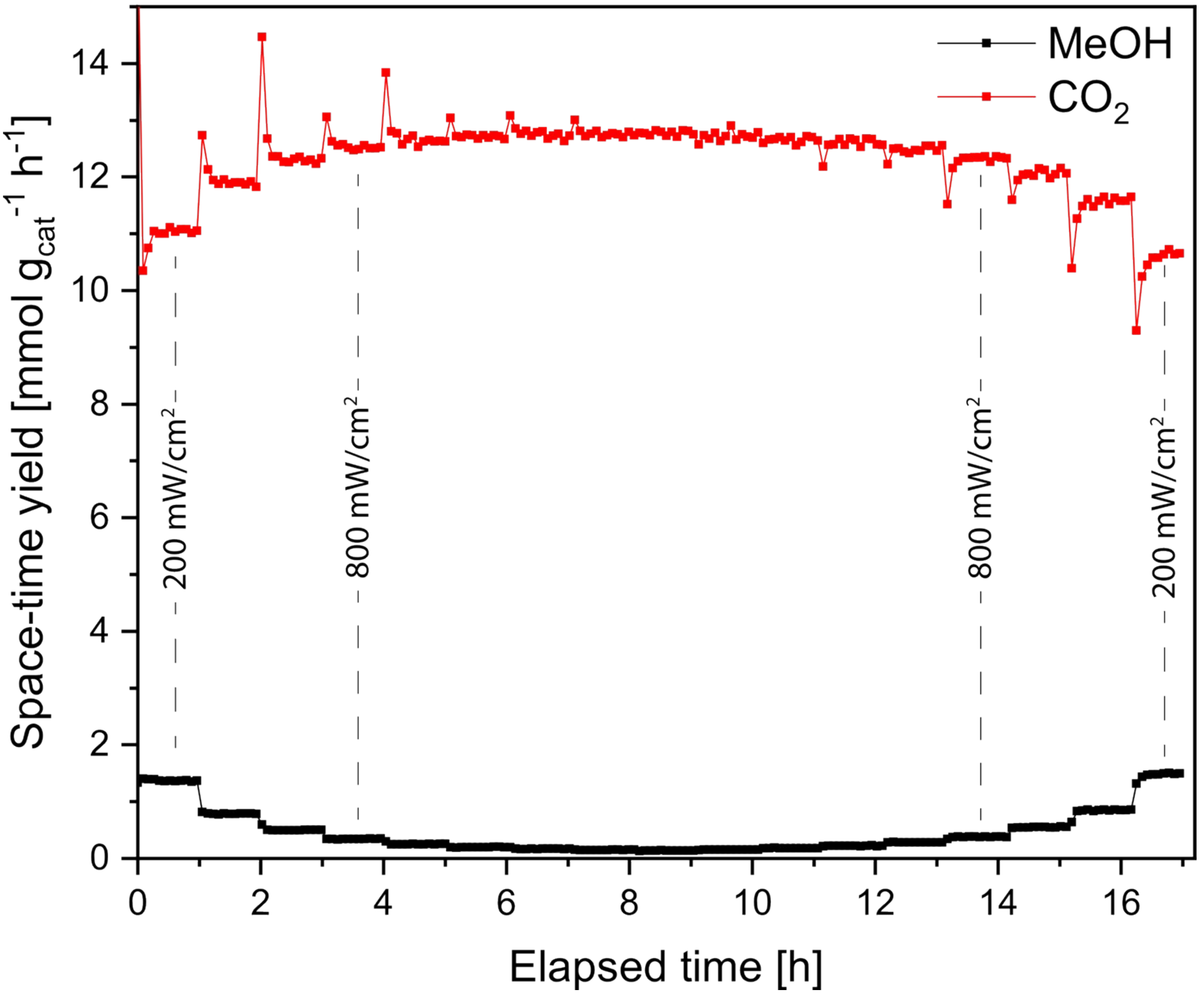

Figure S2 Space-time yield (STY) of methanol (reactant) and CO_2 (product) as a function of time. The reaction was conducted under a total reactant gas flow rate of 20 SCCM with 3% methanol in synthetic air. The light intensity was initially set to 200 mW/cm^2, and then increased in 200 mW/cm^2 increments every hour.

X-ray fluorescence analysis

Table S1 shows the X-ray fluorescence (XRF) elemental analysis of ground aerogels after supercritical drying. Both the TiO_2 and ZrO_2 samples exhibited significant chloride content, originating from the metal chlorides precursors used for synthesis, which release HCl as a by-product upon conversion. The HCl protonates surface hydroxyl groups on the oxide, and the resulting chloride anions physisorb to the positively charged surface. These ions are unlikely to be removed during washing with apolar solvents, solvent exchange, or supercritical drying, leading to a chloride content that correlates with the surface area of the aerogels. The ZrO_2 sample, which has a slightly smaller crystallite size (**Figure 6**) and a higher molar surface area (**Figure 7**), exhibited a higher chloride content. This is partly due to the post-synthetic addition of concentrated HCl solution to achieve stable aqueous colloidal dispersion of ZrO_2 nanoparticles. Additionally, ZrO_2, with its higher isoelectric point (IEP), is more basic and thus may react with more HCl present in the colloidal dispersion. In contrast, the In_2O_3 nanocrystals, synthesized from an acetate precursor without HCl addition, displayed negligible chloride content, as expected.

The chloride content of the untreated TiO_2 aerogel was markedly reduced during the thermal and photocatalytic treatments. Moreover, for the Pd/TiO_2 aerogel, which heat-treated at 350 °C for 20 hours in air before being subjected to photocatalytic reaction conditions, XRF analysis revealed that the palladium (Pd) content was significantly below the nominal value of 1 wt.%. This indicates a low Pd yield during the in-situ synthesis.

Table S1 X-ray fluorescence (XRF) results for the various metal oxide aerogels following supercritical drying, as well as for the Pd/TiO_2 photocatalyst after supercritical drying and subsequent calcination in air at 350 °C.

Sample description	**Metal Oxide [wt.%]**	**Chloride (Cl^-) [wt.%]**	**Palladium (Pd) [wt.%]**
Pure TiO_2 aerogel	96.24	3.76	0
Pure ZrO_2 aerogel	92.62	7.38	0
Pure In_2O_3 aerogel	99.81	0.19	0
Pd/TiO_2 photocatalyst	99.78	0.05	0.17

Scanning transmission electron microscopy (STEM) analysis

The palladium (Pd) nanoparticles were synthesized immediately after the TiO_2 nanocrystals in the same reaction flask, using directly benzyl alcohol as a reducing agent. Efficient catalysts typically require high degree of dispersion and small particle sizes, both of which were assessed by scanning transmission electron microscopy (STEM) supplemented by energy dispersive X-ray (EDX) analysis. **Figure S3** demonstrates the good dispersion of the Pd nanoparticles. Although an in-depth particle size analysis was not conducted, particle sizes ranged from approximately 15 to 60 nm, with most having a diameter of around 25 nm.

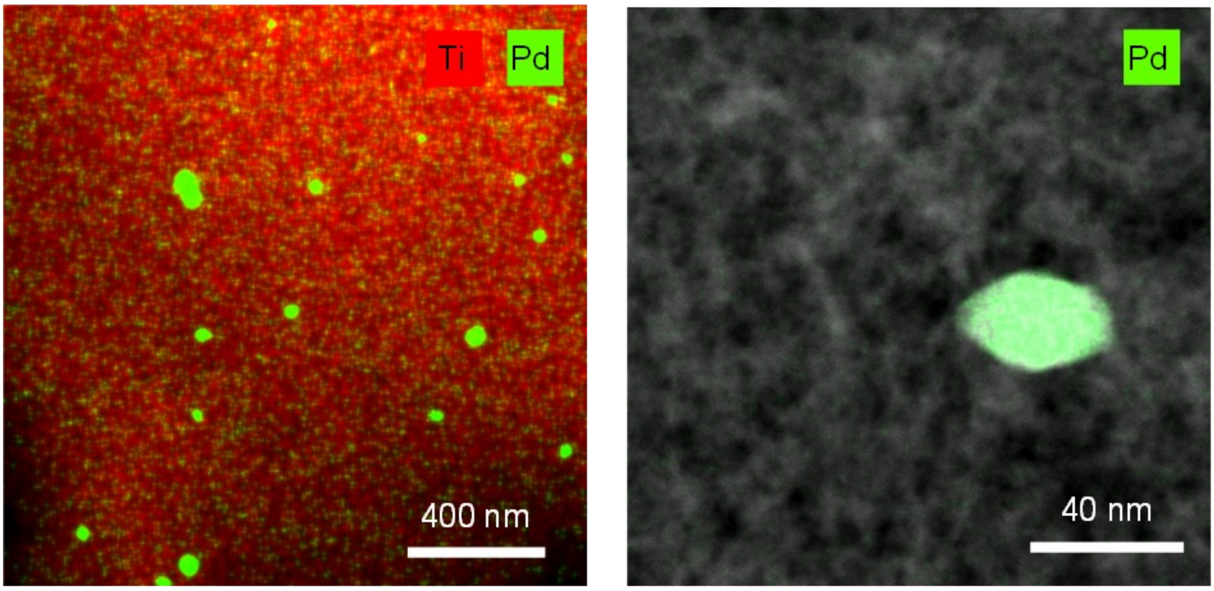

Figure S3 HAADF-EDX images of the Pd/TiO_2 aerogel after supercritical drying. The Pd nanoparticles are well dispersed throughout the TiO_2 aerogel matrix.

The thermal treatment (20 hours at 350 °C in air) used to remove organic and chloride residues did not significantly affect the Pd phase (**Figure S4**). No obvious sintering of the Pd nanoparticles was evident.

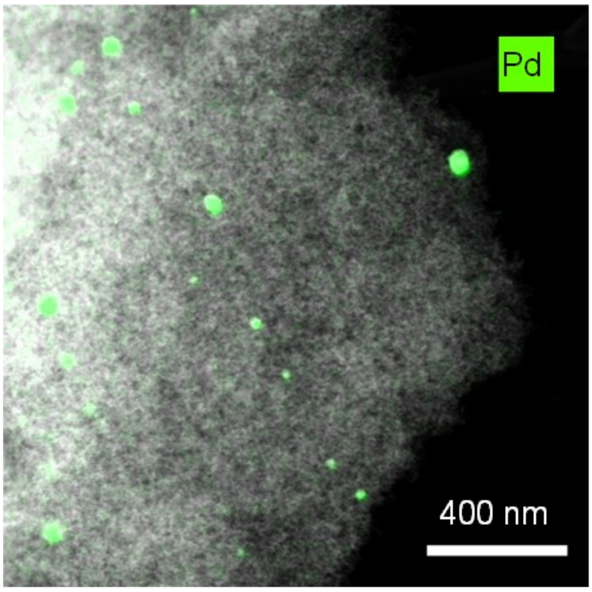

Figure S4 HAADF-EDX images of the Pd/TiO_2 aerogel after thermal treatment at 350 °C for 20 h in air. The Pd nanoparticles are still well dispersed throughout the TiO_2 aerogel matrix.

After several hours of photocatalysis, the photocatalyst displayed a significantly altered morphology. While a few Pd particles around 20 nm in size remained visible, the majority of the Pd phase had dispersed into much smaller nanoparticles, approximately 3 nm in size (**Figure S5**). This observation is unexpected, as catalytic processes typically lead to sintering and the growth of active phase particles, not such extensive dispersion.

However, the phenomenon of particle redispersion is known to occur through deliberate oxidation and subsequent reduction of the catalytic material, leading to the formation of smaller particles and clusters.[2] In this case, the redispersion appears to have occurred spontaneously under the reaction conditions. Spontaneous oxidation and reduction, often referred to as redox dynamics (or redox cycling or oscillatory behaviour) of the active phase, has been observed for unsupported Pd under oxidative conditions and may explain the observed fragmentation and redistribution of the Pd phase.[3-6]

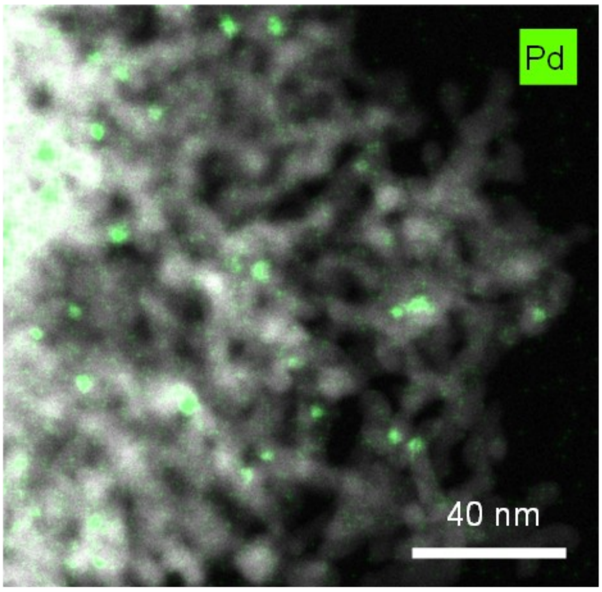

Figure S5 HAADF-EDX images of the Pd/TiO_2 photocatalyst after thermal treatment at 350 °C and photocatalytic experiments. Most of the Pd phase is highly dispersed as small nanoparticles on the TiO_2 aerogel matrix.

Visible light driven photocatalysis

To explore the potential for a photothermal reaction pathway, 365 nm UV LEDs were replaced with white light-emitting LEDs (Thorlabs, MCWHLP1, 400 − 800 nm, 2000 mW cm^{-2}). The spectrum of these visible LEDs is not absorbed by the TiO_2 phase of the catalyst, which shows an absorption onset below 400 nm. Therefore, the primary interaction occurs with the Pd phase. As a result, incident photons are predominantly converted into heat, locally heating the Pd nanoparticles. This thermal energy can drive catalytic reactions, constituting an overall photothermal process.

Figure S6a compares the irradiance-conversion curves under UV and visible light illumination at 20 SCCM and 1% MeOH concentration. Unlike UV light, the visible light curve exhibits an exponential increase in conversion with irradiance, which levels off when reaching full conversion. Such a behaviour is characteristic of thermally driven catalytic processes, as the catalytic activity increases exponentially with temperature.[7] Above approximately 400 mW cm^{-2}, mass transport limitations become significant, leading to saturation in conversion rates and resulting in a sigmoidal shape of the curve. **Figure S6b** shows that the product selectivity under visible light illumination is very similar to the UV light-driven process, with CO_2 selectivity reaching nearly 100% when methanol conversion exceeds approximately 80%.

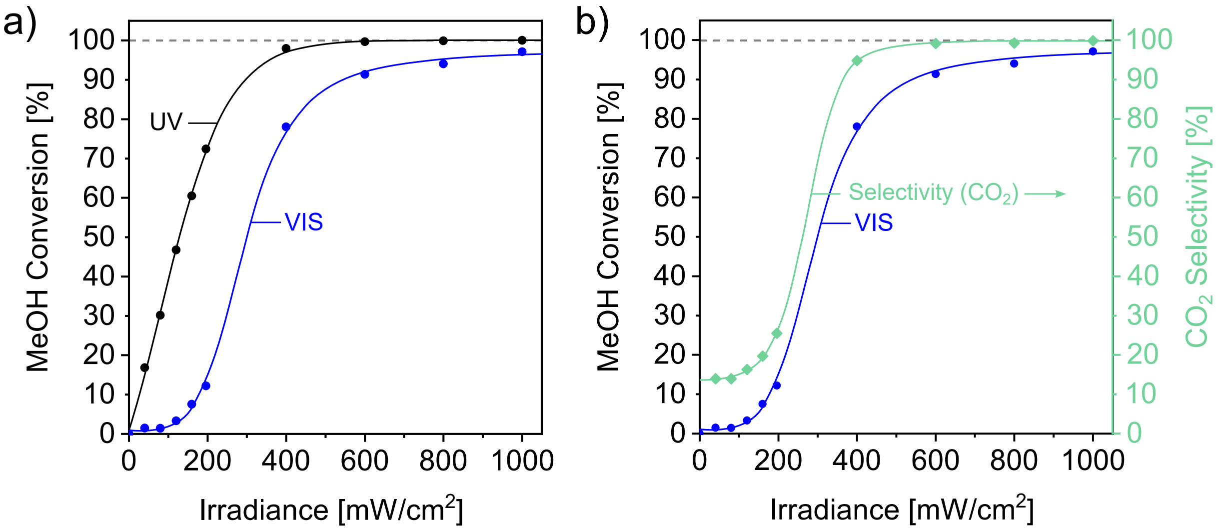

Figure S6 Photocatalytic performance of Pd/TiO_2 worm-shaped granules using different light sources. a) Methanol conversion under UV and VIS illumination. b) Methanol conversion under VIS illumination and the corresponding selectivity for CO_2.

Apparent Quantum Efficiency

The Apparent Quantum Efficiency (AQE) gives an estimate of the efficiency of a photocatalytic reaction by comparing the number of defined events to the number of absorbed photons. We make the simplification that all incident photons reaching the sample are absorbed and thus use the term 'apparent quantum efficiency (AQE)' accordingly. To calculate the number of incident photons, we use the measured LED irradiance and the illuminated catalyst area. We define the photochemical events as the oxidation of methanol's carbon atom by photogenerated holes. To estimate the number of these theoretical oxidations, we consider the oxidation state changes of the carbon atom in each molecule. Specifically, we assume that the conversion of methanol (oxidation state of its carbon atom: C^{2-}) to formaldehyde (C^0) requires two holes per molecule, while complete oxidation to CO_2 (C^{4+}) requires six holes. For the conversion of MeOH to CO_2 and formaldehyde (CH_2O), it can be calculated as follows:

$$AQE(\%) = \frac{utilized\ electrons/holes}{total\ photons} \times 100 = \frac{\left(\dot{N}_{CO_2} \times 6 + \dot{N}_{CH_2O} \times 2\right)}{P \times A \times \frac{\lambda}{h \cdot c}} \times 100$$

where $\dot{N}_{CO_2}$ and $\dot{N}_{CH_2O}$ are the number of CO_2 and CH_2O molecules produced per second, 6 and 2 are the electrons (holes) involved in the oxidation of MeOH to CO_2 and CH_2O respectively, P is the irradiance (in W/cm^2), A is the illuminated area (0.636 cm^2), λ is the wavelength of incident light (365 nm), h is the Planck's constant, and c the speed of light.

$\dot{N}_{CO_2}$ and $\dot{N}_{CH_2O}$ can be calculated from the methanol conversion C_{MeOH} and selectivity towards CO_2 (S_{CO_2}):

$$\dot{N}_{CO_2} = \dot{n}_{MeOH} \times C_{MeOH} \times S_{CO_2} \times N_A$$

$$\dot{N}_{CH_2O} = \dot{n}_{MeOH} \times C_{MeOH} \times (1 - S_{CO_2}) \times N_A$$

where $\dot{n}_{MeOH}$ is the molar flow rate of methanol at the reactor inlet, C_{MeOH} is the fraction of methanol converted by the photocatalyst, S_{CO_2} is the selectivity towards CO_2, (1− S_{CO_2}) is the selectivity towards CH_2O, and N_A is the Avogadro constant. The molar flow rate of methanol $\dot{n}_{MeOH}$ is given by the total gas flow rate (in SCCM, STP: 298 K, 101325 Pa) and the methanol concentration c_{MeOH} at the reactor inlet. For experiments at 20 SCCM with 1% MeOH (1.073% by GC), $\dot{n}_{MeOH}$ is

$$\dot{n}_{MeOH} = \dot{n}_{total} \times c_{MeOH} = \frac{20\,\frac{cm^3}{min}}{60\,\frac{s}{min} \times 24\,464\,\frac{cm^3}{mol}} \times 1.073\,mol\% = 1.46 \times 10^{-7}\,\frac{mol}{s}$$

To evaluate the photocatalytic efficiency of Pd/TiO_2 under UV light, the AQE was calculated for different irradiances (see **Table S2**) using the MeOH conversion and selectivity shown in **Figure 11b**. The AQE is only meaningful if the catalytic process is driven by charge carriers (photocatalytic process) and not by thermal energy (via photothermal effects). To investigate whether the activity under UV light (365 nm) is due to a photocatalytic process, a photothermal effect, or a combination thereof, we compared the methanol conversion under VIS light (400 − 800 nm) and UV light (see **Figure S6**). VIS light is primarily absorbed by the Pd phase, which leads to a local heating of the Pd nanoparticles, inducing a thermal decomposition of MeOH. At the same time, the absorption coefficient of TiO_2 for UV light (365 nm) is very high and the Pd loading only amounts for 0.17 wt.%, making the interaction of UV light with TiO_2 much more likely than with Pd.

Table S2 Irradiance-dependent MeOH conversion at a flow rate of 20 SCCM and 1 % MeOH under UV light (λ: 365 nm) and VIS light (λ: 400 – 800 nm). The Apparent Quantum Efficiency (AQE) under UV light was calculated using the methanol conversion and selectivity towards CO_2 as described above.

Power (mW/cm^2)	**C_{MeOH} (VIS)**	**C_{MeOH} (UV)**	**S_{CO2} (UV)**	**AQE (UV)**
40	1.5%	17%	17%	85%
80	1.4%	30%	18%	77%
120	3.3%	47%	21%	83%
160	7.5%	61%	28%	89%
200	12%	72%	39%	99%
400	78%	98%	98%	110%
600	91%	100%	100%	75%

800	94%	100%	100%	56%
1000	97%	100%	100%	45%

As shown in **Table S2**, VIS light converts only small amounts of methanol (1.4 − 3.3%) at low irradiance (<120 mW cm^{-2}), while MeOH conversions between 17% and 47% are reached for UV light. This leads us to the conclusion that the activity at low irradiance (<120 mW cm^{-2}) is primarily due to photocatalytic and not photothermal processes. This finding is also underpinned by the linear increase in activity with irradiance, which is typical for photocatalytic processes but not for thermal processes. Thermal effects can thus be neglected at low irradiances (<120 mW cm^{-2}), resulting in meaningful AQEs. Remarkably high AQE values of 77 – 83% are obtained within this initial regime, demonstrating that the Pd/TiO_2 aerogels use UV light very efficiently and exhibit low charge carrier recombination. We attribute this finding to the aerogel's excellent crystallinity and the very short diffusion paths for charge carriers to reach the particle surface (0 – 1.5 nm for ~3 nm TiO_2 particles), both of which reduce charge carrier recombination. The AQE increases significantly at irradiances >200 mW cm^{-2}, and even exceeds 100% at 400 mW cm^{-2}, indicating that photothermal effects contributes to the activity at irradiance levels >200 mW cm^{-2}. This observation is in line with the measurements under VIS light, where the activity also increases markedly between 200 – 400 mW cm^{-2} (**Figure S6b**). When approaching full conversion of MeOH, the AQE decreases as expected because the surplus of charge carriers only leads to marginal improvements in conversion. Consequently, the AQE loses its significance at higher irradiance as thermal processes become more prominent and the conversion reaches its limit.

Thermally Induced Sintering of TiO_2 Aerogels

Due to their nanocrystalline nature, nanoparticle-based aerogels are susceptible to sintering at elevated temperatures. This process leads to the growth of nanoparticles, resulting in a significant loss of surface area. Consequently, heating is typically avoided to preserve the aerogel's large initial surface area. However, calcination is often employed to remove organic residues, counter ions (such as nitrates), and adsorbed water from the catalyst's surface. Additionally, many catalytic reactions occur at elevated temperatures, making some degree of sintering and surface area loss inevitable for aerogel-based catalysts. To assess the extent of sintering and surface area reduction, TiO_2 aerogels were treated at various temperatures for 24 hours in air. Post-treatment, the crystallite sizes were estimated using X-ray diffraction (XRD) data analyzed via the Scherrer equation, while surface area measurements were conducted through nitrogen sorption experiments to determine the density functional theory (DFT) surface area (A_{DFT}). Furthermore, the theoretical surface area (A_{calc}) was calculated based on the measured crystallite sizes and the bulk density of TiO_2 (3.88 g cm^{-3}) (**see Table S3**).

In general, the results show a clear trend of increasing crystallite size and decreasing surface area with higher treatment temperatures, consistent with typical sintering behavior. At 100 °C, no sintering occurs, and the crystallite size corresponds to the as-synthesized crystallite size. However, at temperatures above 100 °C, sintering and crystallite growth become evident, accompanied by a gradual reduction in surface area. The similarity observed between A_{DFT} and A_{calc} can be attributed to the highly branched structure of the aerogel, where contact areas between nanocrystals are small. Additionally, the calculated surface area (A_{calc}) does not account for potential polydispersity in nanocrystal size, where smaller nanocrystals can disproportionately contribute to the overall measured surface area (A_{DFT}).

Table S3 Surface area of TiO_2 aerogel monoliths treated for 24 h at different temperatures.

Temperature (°C)	A_{DFT} ($m^2\ g^{-1}$)	Cristallite Size (nm)	A_{calc} ($m^2\ g^{-1}$)
100	512	3.1	499
200	412	3.5	442
300	279	5.3	292
400	226	7.5	206
500	173	10.6	146

The surface area determined by nitrogen sorption analysis gradually decreases at higher temperatures (Table S3), which can be attributed to sintering effects. An increase in crystallite sizes was also observed in the XRD patterns by applying the Scherrer equation on the (101) reflection. The theoretical surface areas derived from the crystallite size and bulk density of TiO_2 show a similar trend to the surface area obtained from gas sorption analysis.

REFERENCES

(1) Luna, A. L.; Papadopoulos, S.; Kyburz, T.; Tervoort, E.; Novotny, L.; Niederberger, M., Insights into light and mass transport in nanoparticle-based aerogels: the advantages of monolithic 3D photocatalysts. *J. Mater. Chem. A* **2021,** *9*, 22380-22391.

(2) Morgan, K.; Goguet, A.; Hardacre, C., Metal Redispersion Strategies for Recycling of Supported Metal Catalysts: A Perspective. *ACS Catal.* **2015,** *5*, 3430-3445.

(3) Yue, S.; Praveen, C. S.; Klyushin, A.; Fedorov, A.; Hashimoto, M.; Li, Q.; Jones, T.; Liu, P.; Yu, W.; Willinger, M.-G.; Huang, X., Redox Dynamics and Surface Structures of an Active Palladium Catalyst during Methane Oxidation. *Nat. Commun.* **2024,** *15*, 4678.

(4) Stötzel, J.; Frahm, R.; Kimmerle, B.; Nachtegaal, M.; Grunwaldt, J.-D., Oscillatory Behavior during the Catalytic Partial Oxidation of Methane: Following Dynamic Structural Changes of Palladium Using the QEXAFS Technique. *J. Phys. Chem. C* **2012,** *116*, 599-609.

(5) Zhang, X.; Lee, C. S. M.; Mingos, D. M. P.; Hayward, D. O., Oscillatory Behaviour during the Oxidation of Methane over Palladium Metal Catalysts. *Appl. Catal. A: Gen.* **2003,** *240*, 183-197.

(6) Bychkov, V. Y.; Tulenin, Y. P.; Gulin, A. A.; Korchak, V. N., Catalytic Properties and Structure of Palladium Surface Layer Formed in the Course of a Self-Oscillatory Reaction of Methane Oxidation. *Kinet. Catal.* **2022,** *63*, 312-320.

(7) Baffou, G.; Bordacchini, I.; Baldi, A.; Quidant, R., Simple Experimental Procedures to Distinguish Photothermal from Hot-Carrier Processes in Plasmonics. *Light. Sci. Appl.* **2020,** *9*, 108.